

Adaptive Response of Actin Bundles under Mechanical Stress

Florian Ruckerl,^{1,2} Martin Lenz,³ Timo Betz,^{1,2} John Manzi,^{1,2} Jean-Louis Martiel,⁴ Mahassine Safouane,^{1,2} Rajaa Paterski-Boujemaa,⁴ Laurent Blanchoin,^{4,*} and Cécile Sykes^{1,2,*}

¹CNRS, Laboratoire Physico Chimie Curie, Institut Curie, PSL Research University, Paris, France; ²Sorbonne Universités, UPMC University Paris 06, Paris, France; ³CNRS, LPTMS, University Paris-Sud, Orsay, France; and ⁴CNRS/CEA/INRA/UJF, Laboratoire de Physiologie Cellulaire Végétale, Institut de Recherches en Technologies et Sciences pour le Vivant, Grenoble, France

ABSTRACT Actin is one of the main components of the architecture of cells. Actin filaments form different polymer networks with versatile mechanical properties that depend on their spatial organization and the presence of cross-linkers. Here, we investigate the mechanical properties of actin bundles in the absence of cross-linkers. Bundles are polymerized from the surface of mDia1-coated latex beads, and deformed by manipulating both ends through attached beads held by optical tweezers, allowing us to record the applied force. Bundle properties are strikingly different from the ones of a homogeneous isotropic beam. Successive compression and extension leads to a decrease in the buckling force that we attribute to the bundle remaining slightly curved after the first deformation. Furthermore, we find that the bundle is solid, and stiff to bending, along the long axis, whereas it has a liquid and viscous behavior in the transverse direction. Interpretation of the force curves using a Maxwell visco-elastic model allows us to extract the bundle mechanical parameters and confirms that the bundle is composed of weakly coupled filaments. At short times, the bundle behaves as an elastic material, whereas at long times, filaments flow in the longitudinal direction, leading to bundle restructuring. Deviations from the model reveal a complex adaptive rheological behavior of bundles. Indeed, when allowed to anneal between phases of compression and extension, the bundle reinforces. Moreover, we find that the characteristic visco-elastic time is inversely proportional to the compression speed. Actin bundles are therefore not simple force transmitters, but instead, complex mechano-transducers that adjust their mechanics to external stimulation. In cells, where actin bundles are mechanical sensors, this property could contribute to their adaptability.

INTRODUCTION

The actin cytoskeleton is an essential component of the cell, and plays an important role in many dynamic processes involving cell motility and cell shape changes (1–4). Indeed, actin assembly into higher-order structures is a prerequisite for force transduction and the regulation of cellular shape (4,5). Bundling of actin filaments is crucial for the function of cytoskeletal elements such as filopodia, stress fibers, or the contractile ring (6–8). The main focus of experimental and theoretical investigations has been the mechanical properties of filamentous actin (F-actin) networks (9–11). In these studies, actin filaments are considered as passive semi-flexible polymers that confer mechanical properties onto the network depending on its specific organization. However, it has recently been shown that a single actin filament is not a

passive polymer. Instead, F-actin undergoes structural transitions when put under tension, and this phenomenon might explain different affinity of actin filaments with interacting proteins (12,13). F-actin bundles themselves have been less thoroughly investigated, although bundled F-actin exists in a variety of states in cells. However, F-actin bundles may also undergo changes when under stress, and may not behave like simple beams, but, instead, display distinctive collective properties resulting from their interactions (14). In cells, F-actin bundles are produced by a variety of transiently cross-linking proteins including fascin, fimbrin, and α -actinin. Direct investigation of the mechanical properties of F-actin bundles in vitro, focusing on the important role played by bundling proteins, has been developed by various groups (15–17). Actin networks cross-linked by α -actinin display strain hardening at high cross-linker concentrations (18,19). Analysis of thermal fluctuations of rings of cross-linked F-actin bundles allows us to access bundle stiffness as a function of cross-linker types and concentrations (20,21). Direct manipulation of individual actin

Submitted February 28, 2017, and accepted for publication July 31, 2017.

*Correspondence: laurent.blanchoin@cea.fr or cecile.sykes@curie.fr

Florian Ruckerl and Martin Lenz contributed equally to this work.

Editor: Enrique De La Cruz.

<http://dx.doi.org/10.1016/j.bpj.2017.07.017>

© 2017 Biophysical Society.

This is an open access article under the CC BY-NC-ND license (<http://creativecommons.org/licenses/by-nc-nd/4.0/>).

bundles reveals elastic and elasto-plastic properties of the bundles at different timescales (22). In cells, specific nucleators of actin polymerization such as formins form parallel bundles (23). In vitro, these bundles can also be reproduced without specific cross-linkers, using methyl-cellulose or PEG as a depletion force agent, or a multivalent cation (MgCl_2) to enhance the electrostatic interaction between the filaments. Such bundles have interesting properties, as they are able to retract after being expanded longitudinally (24), and two actin filaments are able to zipper into a bundle with a force on the order of tenths of piconewtons (25). How weak bonds between the filaments, in the absence of cross-linkers, can impact the mechanical properties of the whole bundle under compression, has not been addressed.

Here, we apply large, cyclic deformations of individual bundles of actin filaments created by unspecific depletion agents like methyl cellulose and divalent cations Mg^{2+} . Deformations are applied using an optical tweezers setup to hold the actin bundle at both ends. Our measurements show that the cyclic deformations lead to a decrease in the force necessary to buckle the bundle, which reveals, to our knowledge, a new mechanical behavior of actin bundles. These results can be understood in the framework of a visco-elastic model, demonstrating that the bundle undergoes internal rearrangement under forcing, revealing the magnitude of the adhesion and friction forces between the filaments.

MATERIALS AND METHODS

Multiplexed optical tweezers setup

Two digital acousto-optical deflectors (DTSXY-400-1064; AA Opto Electronic, Orsay, France) control the x - y position of the laser in a custom-built setup (see Fig. S4). They are used to create two optical traps in time-sharing mode at a switching rate of 20 kHz using a digital controller (DDSPA2X-D423b-34-0dB; AA Optoelectronics). The continuous wave IR-laser beam (YLM-1-1064-LP; IPG Photonics, Oxford, MA) is widened to slightly overfill the back aperture of the focusing objective (UPLSAPO60XW/IR, NA 1.2, 60 \times , water immersion; Olympus, Melville, NY) and the light is collected by a long distance objective (60 \times , water immersion, LUMPLFL 60 \times , NA 0.9; Olympus). A four-quadrant photodiode (QPD; Cat. No. G6849; Hamamatsu, Hamamatsu City, Japan) is connected to an amplifier (Öffner MSR-Technik, Plankstadt, Germany) to detect the position of trapped beads. Two controllers (PCIe-6259 and NI PCIe-6363; National Instruments, Austin, TX) are used for data acquisition and setup control, allowing a sampling rate of 500 kHz per channel of the QPD. The control of the setup and the analysis of the data are realized using the softwares LabVIEW 2010 (National Instruments) and MATLAB 2011b (The MathWorks, Natick, MA).

QPD and trap calibration

The conversion of QPD voltage into spatial position of the trapped bead is done with a calibration procedure that consists of scanning the laser trap over the bead, similarly to a scan over the membrane as done in (26). The bead is first trapped for 40 μs at a reference position, and then the trap is moved to a position along the centerline for 4 μs during which the QPD signal is recorded and averaged. Next, the trap is put back to the reference position for 40 μs before the next scan point is measured. This

stepwise scanning is repeated until a complete linescan through the center of the bead is finished. Typically, the scan has a step size of 10 nm and spans the whole diameter of the bead. To avoid systematic errors, subsequent scan points were on opposite sides with respect to the bead. Close to the bead center (± 500 nm) the signal at the QPD depends linearly on the distance between the trap and the bead center (Fig. S1). This linear regime allows converting the normalized voltage of the QPD into the spatial distance of bead to trap with subnanometer accuracy, determined from the noise floor. Finally, the trap stiffness is obtained from the power spectral density of the bead fluctuations using an adapted version of the method described by Berg-Sørensen and Flyvbjerg (27) (see Fig. S1 d).

Protein preparation

Globular actin is obtained from powder (Cat. No. AKL99; Cytoskeleton, Denver, CO) resuspended in G-Buffer (5 mM TRIS, 0.2 mM CaCl_2 , 0.2 mM ATP) at a concentration of 30 μM . Fluorescent actin (Alexa Fluor 488 Conjugate, Cat. No. A12373; Invitrogen, Carlsbad, CA) is added at a fraction of 12 mol %. The actin solution is stored on ice overnight to allow the remaining F-actin to depolymerize, and is used for up to one week. Formin (Gst-mDia1-FH1-FH2-His, called “mDia1” in the following) is purified following the protocol described in (28,29). The mDia1 is stored at -80°C and thawed directly before use. Cap- $\alpha\beta$ is expressed following the protocol described by Soeno et al. (30) and stored in glycerol at -20°C . Profilin is obtained as described in Lu and Pollard (31) and stored on ice.

Bead functionalization with mDia1-FH1-FH2

The freshly thawed mDia1 is diluted in X-Buffer (10 mM HEPES, 100 mM KCl, 1 mM MgCl_2 , 0.1 mM CaCl_2) to a final concentration of 2 μM . A volume of 5 μL of carboxylated latex beads (Cat. No. 17140, 4.5 μm ; Polysciences, Warrington, PA) is washed in 100 μL pure water and centrifuged for 2 min at 5000 $\times g$. Sedimented beads are then suspended in the mDia1 solution, and incubated for 30 min on a temperature-controlled shaker (20 $^\circ\text{C}$, 750 Rpm). Coated beads are then centrifuged (5000 $\times g$, 2 min, 4 $^\circ\text{C}$) and the sediment suspended in 100 μL of X-Buffer with additional 1% of BSA (Cat. No. A7906; Sigma-Aldrich, St. Louis, MO). After 10 min of incubation on ice, the solution is again centrifuged (5000 $\times g$, 2 min, 4 $^\circ\text{C}$) and the beads resuspended in 50 μL X-Buffer with additional 0.1% BSA. Prepared beads are stored on ice and used over the next three days.

Sample preparation

The proteins (final concentrations 3.1 mM actin, 9.7 mM profilin, 1 nM Cap- $\alpha\beta$) are prepared in a buffer containing 10 mM HEPES, 85 mM KCl, 13 mM NaCl, 0.3% BSA, 1.3 mM DTT, and 1.3 mM DABCO. Just before the transfer to the setup, ATP, methyl cellulose, and MgCl_2 are added to yield a final concentration of 0.5 mM ATP, 0.15% methyl cellulose, and 0.5 mM MgCl_2 , respectively. Of this solution, 12 μL are deposited on a large cover slide (Cat. No. 1; 24 \times 60 mm; Menzel-Gläser, Thermo Fisher Scientific, Waltham, MA) previously cleaned with ethanol. A smaller, also cleaned, cover slide (Cat. No. 1, 18 \times 18 mm; Menzel-Gläser, Thermo Fisher Scientific) is placed on top of it and carefully pressed down to remove bubbles. The chamber is then sealed using a 1:1:1 mixture of Vaseline/lanolin/paraffin. In a typical experiment, one bead is optically trapped and the QPD voltage is calibrated into position as described above. Note that the focused laser beam leads to concentrating actin around the beads, which we exploit to influence the direction of the bundle: we move the trap (or the stage) with a velocity of ~ 5 $\mu\text{m/s}$ toward one side of the actin cloud, where actin bundle growth is induced. A second bead is attached to the bundle by utilization of a second optical trap, leading to an individual

bundle attached to two independently movable traps (see Fig. 1). Repeated calibration shows that the additional diffraction of actin does not change the behavior of the trap. After the polymerization has stopped (~30 min), the traps are aligned horizontally or vertically to simplify later analysis. One trap is then used to move the bead and, thereby, to deform the bundle by either compression or elongation, whereas the second, immobile trap is used as the measuring trap.

RESULTS AND DISCUSSION

To generate actin bundles, molecular crowding is obtained by using methyl-cellulose as a depletion agent, and electrostatic interaction between actin filaments is obtained by the use of multivalent ions ($MgCl_2$) (32). Actin filaments are grown from the surface of mDia1-coated latex beads (28,29), and self-organize into bundles of 20–40- μm length. Beads are optically trapped and provide handles to manipulate the bundle. After 30–90 min of incubation, two mDia1-coated beads are brought close by, and their actin filaments gather into a single bundle. The force on the beads is calibrated before each experiment (Fig. S1 and Materials and Methods), and subsequently measured on

both beads simultaneously while manipulating the bundle. Holding the undeformed bundle in place does not show any change in force. Note that whereas single actin filaments generated by mDia1 detach from the nucleator (28), here, the whole bundle remains attached to the bead, likely through a cooperative phenomenon of a group of filaments being still attached although others detach. We thus perform the following compression/extension protocol (Fig. 1). The entire stationary bundle is first held straight for at least 10 s at zero force, which corresponds to the beads being centered in the traps. One trap is then moved toward the other at a constant absolute speed between 0.25 and 20 $\mu m/s$ (Fig. 1, yellow area). The force initially increases roughly linearly with time (Fig. 1 d, red curve, after $t = 10$ s), corresponding to a slight longitudinal compression of the bundle (Fig. 1 d, dashed and blue line, respectively). As the compressive force exceeds a certain threshold of the order of 5 pN, the bundle buckles as observed in video microscopy (Fig. 1 f) and reflected in the shoulder and following plateau in the force curve. As the beads are brought even closer together, the bundle

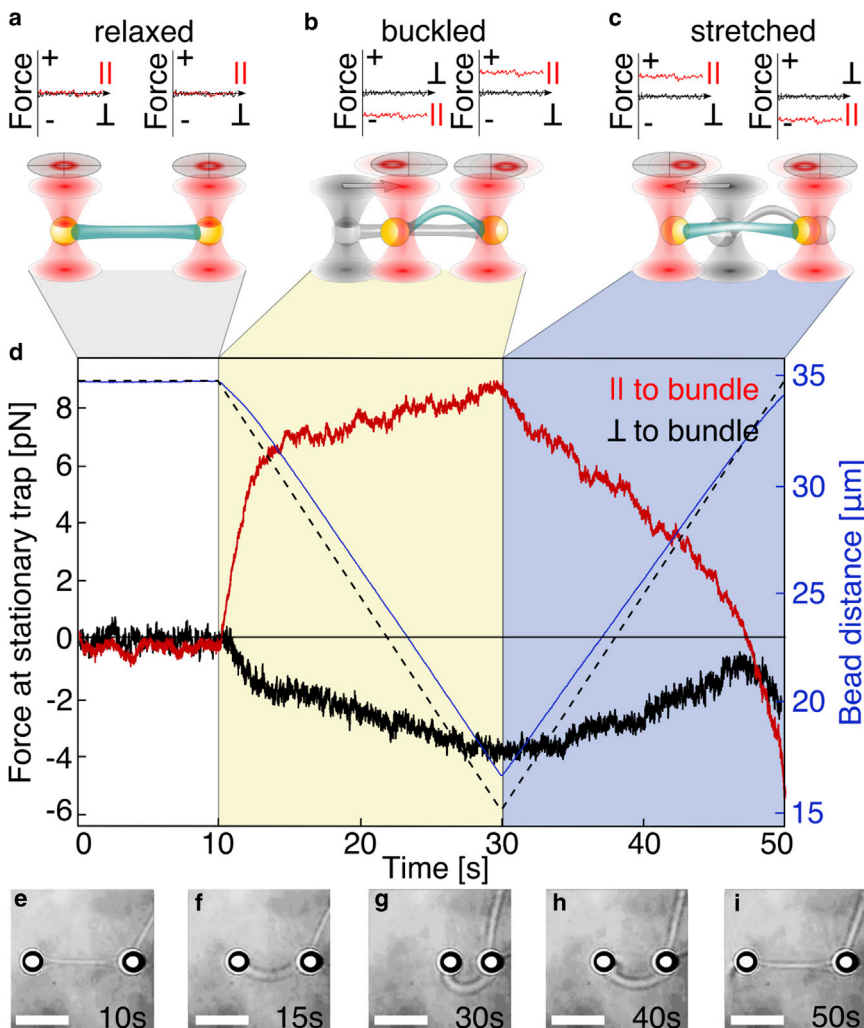


FIGURE 1 Deformation of an actin bundle at a velocity of 1 $\mu m/s$. (a) The bundle, attached to two beads trapped in optical tweezers, is held at zero force. (b) One trap is then moved closer to the second one (yellow area), consecutively compressing (steep slope after $t = 10$ s), buckling (shoulder at $t = 12$ s), and finally bending the actin bundle (slight increase of force). (c) The traps are moved away from each other, reversing the deformation (blue area, negative slope of force) until they reach their initial positions. The sign of the force, positive or negative, indicates directionality, pointing outward or inward, respectively. (a–d) The red and black data curves are the force parallel and perpendicular to the motion, respectively. The nonzero perpendicular force originates from the off-center fixation of the bundle on the bead. The dashed line indicates the distance between the traps, whereas the actual distance between the beads is shown as the blue line. The phase contrast images (e–i) illustrate the aspect of the bundle at different positions in the cycle, indicated by the time in the lower-right corner. The scale bar represents 15 μm .

becomes increasingly bent and the force increases slowly, as expected for a rigid beam (Fig. 1 *d*, $t = 15\text{--}30$ s). The displacement of the beads is stopped when their distance is approximately one-half the initial bundle length, after which we immediately start moving the trap centers apart with the same absolute speed (Fig. 1, *blue area*). During this expansion phase, the curvature of the bundle relaxes and the force decreases. Traps are moved until they reach their initial position, but the striking observation is that the beads themselves do not return all the way back to their initial positions. Indeed, the distance between the two beads at that time is 670 nm smaller than the initial distance, implying that the bundle is under tension, and pulling is apparent from the negative sign of the force at the end of the expansion phase (Fig. 1). This observation indicates that the compression-extension process alters bundle shape and mechanics.

To assess whether further bundle modifications can be induced, we repeat this compression-extension process several times. Strikingly, the subsequent cycles differ from the first one in several respects (Fig. 2). First, the shoulder in the force curve upon buckling becomes less and less pronounced (Fig. 2, *a* and *b*, *blue curves*) compared to the first cycle (Fig. 2, *a* and *b*, *black curves*). The maximal and minimal forces reached at the end of the compression and extension phases only slightly change from cycle to cycle (*red lines*, Fig. 2 *a*, $\pm 0.3\text{pN}$, and non-systematically (no trend)). The similarity of the curves between the second and the fifth cycles shows that the system rapidly settles into a steady state after the first buckling event. All these observations are a robust feature of the system, as confirmed by experiments at different trap speeds (Fig. S2). Plotting the force as a function of displacement for the compression and extension phases, we find that they do not overlap, indicating irreversible bundle deformation (*inset* of Fig. 2 *b*). We measure the hysteresis from the data by numerically calculating the difference between the integral of the compression and the expansion cycle. We find that the energy dissipated over the first hysteresis cycle substantially decreases in subsequent cycles.

To rationalize our observations, we attribute the irreversible bundle deformation and hysteresis to changes in the internal structure of the bundle. We describe these changes using a Maxwell viscoelastic model for extensional and bending deformations of the bundle (Fig. 2 *c*) with three adjustable parameters: a viscoelastic time τ , a 1D stretching modulus (i.e., the characteristic force required to induce a strain of order one) k_s , and a bending modulus κ . On timescales shorter than τ , the filaments and the bonds between them are strained reversibly, therefore the bundle responds elastically on short timescales as characterized by k_s and κ ; on timescales longer than τ , the resulting bond stress relaxes as the bonds are broken and reformed, resulting in relative sliding of the filaments; the bundle flows viscously

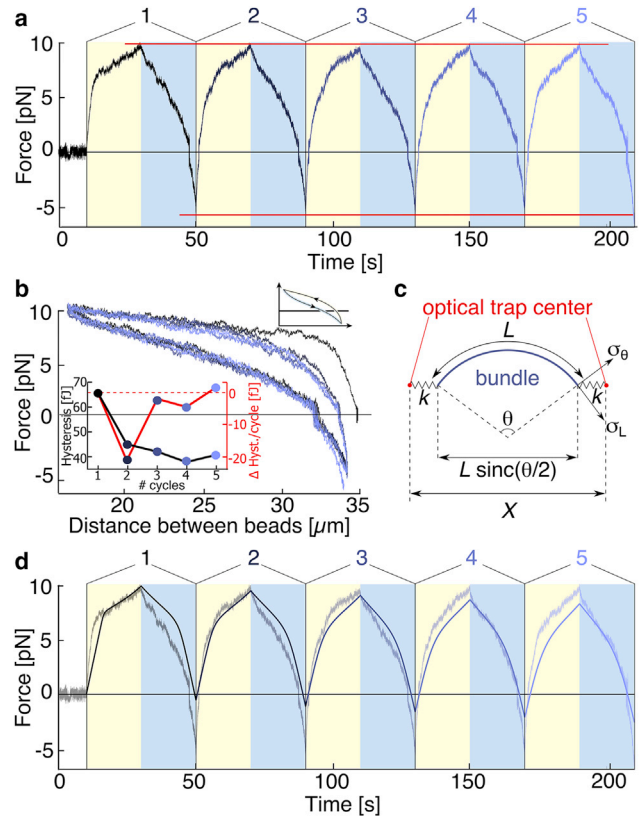


FIGURE 2 Series of five consecutive deformations at $1\ \mu\text{m/s}$. (a) Force-time traces of five consecutive deformations as described in Fig. 1; the force shown is the longitudinal component of the force acting on the trap. A negative force corresponds to a situation where the traps are further apart than the beads, i.e., the exerted force is pulling on the bundle. A positive force denotes pushing on the bundle. Individual cycles are shown in different shades of blue, from black (first cycle) to light blue (last cycle). Yellow and blue regions correspond to compression and expansion periods, respectively. (b) Force-distance curves of the bundle deformation during the cycles. In the compression period, shown by the upper curves, the traps move from right to left; in the expansion periods, shown by the lower curves, the traps move from left to right. The inset is a scheme to show the direction of the hysteresis. (c) Schematic of the model used for fitting the data. L denotes the initial length of the bundle, $X(t)$ is the distance between the traps, and k is the trap stiffness. The bundle tension is denoted by σ_L and the bending torque by σ_θ . (d) Comparison between the fit (continuous line) and the original data yield good overall agreement. One set of parameters τ , k_s , and κ is used to fit the whole curve (see Table S1).

in the longitudinal direction, implying a change in its resting length and the acquisition of a spontaneous curvature, as filaments slide past each other at its cross section.

We model the actin bundle as a viscoelastic beam and approximate its shape to a circular arc. Introducing the bundle length L and bending angle θ (see Fig. 2 *c*), the extension and bending dynamics are each described by a Maxwell model, as a function of time t , as follows, in the longitudinal direction:

$$\frac{k_s}{L_0} \frac{dL}{dt} = \frac{d\sigma_L}{dt} + \frac{\sigma_L}{\tau}, \quad (1a)$$

and in the transverse direction:

$$\frac{\kappa}{L_0} \frac{d\theta}{dt} = \frac{d\sigma_\theta}{dt} + \frac{\sigma_\theta}{\tau}, \quad (1b)$$

where σ_L is the bundle tension (force conjugate to L), σ_θ is its bending torque (conjugate to θ), and L_0 is its initial length. The bundle is subjected to a longitudinal compressive force f applied by the optical tweezers, and force balance in the longitudinal and angular directions yields

$$\sigma_L = -f \operatorname{sinc} \theta/2, \quad (2a)$$

$$\sigma_\theta = \frac{fL}{\theta} (\operatorname{sinc} \theta/2 - \cos \theta/2), \quad (2b)$$

where the *sinc* function is defined by $\operatorname{sinc}(x) = \operatorname{sinc}(x)/x$. In the experiments, the distance $X(t)$ between the centers of the two optical traps is imposed by the operator. Each bundle end, bound to a bead, is thus confined to the vicinity of the center of one of the traps through a harmonic restoring force with spring constant $k = 19 \text{ pN}/\mu\text{m}$ equal to the trap stiffness. Using the fact that the distance between bundle ends reads ($L \operatorname{sinc} \theta/2$), the longitudinal force plotted in Fig. 2 is given by Hooke's law as

$$f = \frac{k}{2} [X(t) - L \operatorname{sinc} \theta/2], \quad (3)$$

where the factor 1/2 is due to the presence of two traps in series. In the following, we predict the time dependence of this force for a given protocol $X(t)$ by solving the system of Eqs. 1–3 numerically, as described in the [Supporting Materials and Methods](#).

The model is able to qualitatively capture our observations, as shown by fitting the force curve of Fig. 2 *a* using τ , k_s , and κ as adjustable parameters (Fig. 2 *d*) as well as other experimental force curves at different compression velocity, with one set of parameters for each bundle (Fig. S2). As the initial configuration of the bundle is devoid of spontaneous curvature, its response to the first round of compression displays a sharp buckling threshold, reminiscent to that of a straight rod. Once the bundle is curved, its internal reorganization process begins and spontaneous curvature builds up. As in the experiment, the buildup of spontaneous bundle curvature requires the exertion of a negative (pulling) force to stretch it back to its initial length. When the second round of compression begins, the buckling transition is blunted. Over the following rounds of compression-extension, the spontaneous curvature of the bundle builds up, and thus the maximum force required for compression decreases, whereas an increasingly large negative force is required to stretch it back to its initial length. However, the absolute value of this negative force is greater in the experiments than in the model, suggesting some reor-

ganization effects that are not taken into account in the model (see below). After a time on the order of the viscoelastic timescale τ , the bundle settles into a steady state as observed experimentally. Note that this viscoelastic time is found to be inversely proportional to the compression speed (Fig. S6). In fact, the bundle is initially compressed longitudinally (Fig. 1 *d* and S2) before it buckles. Assuming that the critical strain required for buckling is similar in all experiments presented in Fig. S2, the time to reach it (that we call the “visco-elastic time”) will indeed be inversely proportional to the bundle compression velocity. Moreover, we assume here that the viscoelastic timescale associated with the curvature of the bundle is identical to that associated with its shortening. Although fitting two different viscoelastic times would improve the fit of the model to the experiment, we found that it does not yield any significant additional physical insights here.

Our proposed picture of viscoelastic bundle relaxation implies that the spontaneous length and curvature of the bundle should relax even in the absence of trap motion. To confirm this, we carried out a second type of measurement that includes two waiting times of typically 30 s, one after the phase of bead approach and one after bead separation. During the waiting phase, traps are fixed at their positions and only the force on the beads is measured. As anticipated, we observe that the force relaxes when the traps are held (Fig. 3). The negative minimal force peak increases much more than in the absence of waiting times over successive cycles (Fig. 3 by +0.7 pN on average), implying that the bundle becomes less and less amenable to stretching and thus that spontaneous curvature builds up over the course of the experiment. In addition, buckling the bundle at the beginning of the compression phase becomes easier in the following cycles, confirming the presence of bundle remodeling, independent of the details of our driving protocol. Note that the model roughly reproduces the trend of the data (Fig. 3 *c*). Although the detailed understanding of how actin bundles reorganize during the waiting time, pictured by the increase in the hysteresis, may imply more complex deformations of the bundle, these are not taken into account in our current model. One possibility could be that the actin bundle undergoes some plastic rearrangements during this waiting time, and breakage of the filaments may increasingly happen during the waiting time. This effect may explain the greater absolute value of the negative force in experiments compared with the model. Further modeling may include this aspect in the future.

To elucidate the microscopic underpinning of our observations, we systematically fit our model parameters for all data obtained in the experiment pictured in Fig. 2. This is a global fit, with one set of parameters for each bundle, therefore covering a wide range of driving velocities and deformation amplitudes ($n = 15$ curves; Table S1). We find a bending rigidity $\kappa = 770 \pm 530 \text{ pN} \cdot \mu\text{m}^2$, corresponding to an average persistence length of $190 \mu\text{m}$, and a bundle stretching rigidity

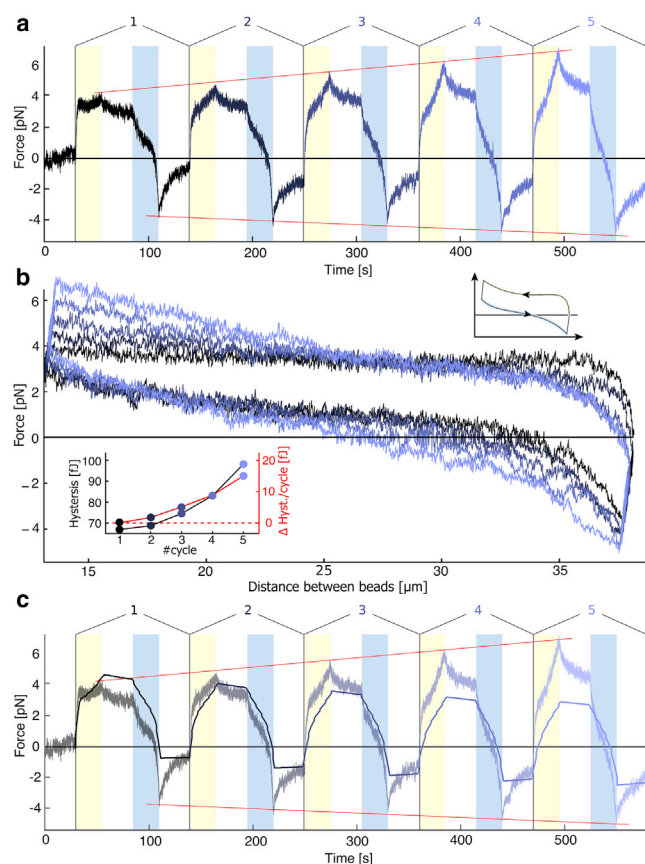


FIGURE 3 Series of five cyclic deformations at an absolute speed of $1 \mu\text{m/s}$ with a relaxation period of 30 s. (a) Shown here are force-time traces of five consecutive deformations, as described in Fig. 1. (b) Shown here are the force-distance curves of the bundle deformation during the cycles. The inset is a scheme to show the direction of the hysteresis. (c) Comparison is given between the fit (continuous line) and the original data.

$k_s = 120 \pm 76 \text{ pN}$. These values support a simple mechanical model where the bundle is constituted of weakly coupled filaments, i.e., its filaments are not constrained to strictly remain in register during an elastic deformation (20,33). Indeed, measuring bundle thickness from electron micrographs (Fig. S3) leads to an estimate of the number of filaments per bundle $N = 20,000$ (Supporting Materials and Methods). The weakly coupled model implies a bundle bending rigidity $\kappa = N\kappa^{(1)} \approx 1200 \text{ pN} \cdot \mu\text{m}^2$, where $\kappa^{(1)} \approx 0.06 \text{ pN} \cdot \mu\text{m}^2$ is the bending modulus of a single filament (corresponding to a persistence length $l_p^{(1)} = 15 \mu\text{m}$ (34)). Similarly, the stretching modulus $k_s = Nk_s^{(1)} \approx 86 \text{ pN}$, where we get the stretching modulus of a single filament of length $L_0 = 20 \mu\text{m}$ as $k_s^{(1)} = (90 k_B T l_p^2 / L_0^3)$, as expected from entropic elasticity (35). The estimated values of κ and k_s for weakly coupled filaments are therefore in good agreement with the values obtained from the fit of the experimental data.

This good understanding of the bundle's short-time elastic response enables us to discuss its long-time viscous relaxation as characterized by the viscoelastic time of $\tau = 150 \pm 200 \text{ s}$ (the considerable dispersion-measured

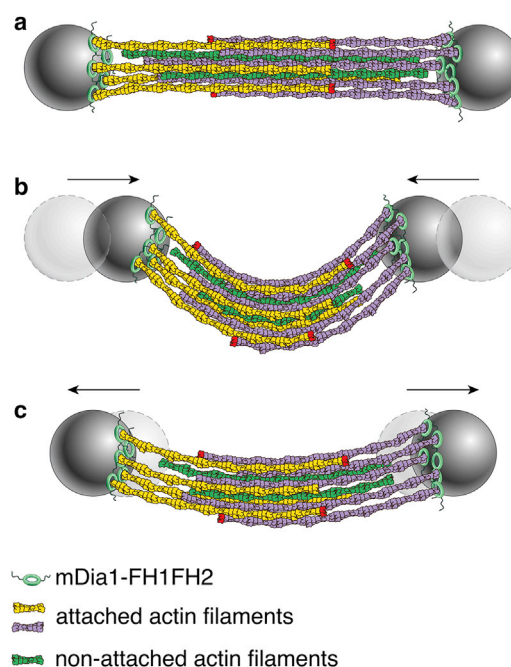


FIGURE 4 Illustration of the microscopic model leading to adaptive mechanics. At rest (a), the bundle is made of parallel and antiparallel filaments. Filaments are connected to mDia beads on one end and have a free end depicted in red. In compression (b), filaments slide and red ends are further apart at the inside of the buckled bundle and closer at the outside. When the bundle is stretched again, there is a memory of the deformation (c) and the bundle does not go back to its initial position.

τ -values are discussed in the Supporting Materials and Methods). As filaments are nucleated on either bead, any single filament is attached to one bead at most, implying that filaments subjected to sustained forces slide relative to each other (36) (Fig. 4). Such forces arise when the bundle is bent, inducing compression on the inner face of the bundle (that with the largest curvature), and extension on the opposite side (Fig. 4). As filaments slide relative to each other, the outer face of the bundle thus extends and the inner face shortens. This differential extension is equivalent to the acquisition of a spontaneous bundle curvature, as described by Eq. 1 b. From a macroscopic perspective, the viscoelastic time τ can be viewed as the ratio of friction and elasticity in the bundle, reflecting the fact that both small friction and strong elastic restoring forces drive speedy viscoelastic relaxation. Following this idea, a simple model of force relaxation inside the bundle allows us to infer a value for the interfilament friction coefficient ζ from our experimental measurement of τ , yielding $\zeta = (8 k_s \tau / L_0^2) \approx 117 \text{ pN} \cdot \text{s} \cdot \mu\text{m}^{-2}$. This value is on par with the friction forces measured for two filaments in the absence of bundling (36) (Supporting Materials and Methods and Fig. S5).

The static mechanics of actin bundles have previously been investigated under a wide range of conditions in the presence of cross-linkers. However, their dynamical behavior as well as

the role of other physical interactions are still poorly understood. In this study, we reveal that molecular crowding and electrostatic interactions lead to weak elastic coupling between filaments, yet they have strong dynamic friction. As the bundle undergoes cyclic deformation, these interactions lead to changes in its internal structure and mechanical properties, leading it to behave as an adaptive material under mechanical stress. Cells may exploit these properties and the associated diminished bundle buckling force when probing their surroundings using their filopodia, much like snails retracting their antennae when sensing an obstacle. Moreover, the striking mechanical behaviors of actin bundles we uncover here could inspire artificial force probes able to sense force once, transmit information, and conserve the memory of the deformation corresponding to the sensed force.

SUPPORTING MATERIAL

Supporting Materials and Methods, six figures, and one table are available at [http://www.biophysj.org/biophysj/supplemental/S0006-3495\(17\)30842-1](http://www.biophysj.org/biophysj/supplemental/S0006-3495(17)30842-1).

AUTHOR CONTRIBUTIONS

C.S. and L.B. designed research and wrote the article. M.L. developed modeling and wrote the article. F.R. carried out and developed experiments and analysis, and wrote the article. R.P.-B. carried out and developed experiments. J.-L.M. contributed to modeling. M.S. contributed to the experimental development. J.M. performed protein purification. T.B. developed the experimental setup and analysis.

ACKNOWLEDGMENTS

Our group belongs to the CNRS consortium CellTiss. We acknowledge Dr. Daniel Lévy for his help in electron microscopy experiments, and Dr. Agnieszka Kawaska at IlluScientia.com for the graphical representation of Fig. 4.

This work was supported by the French Agence Nationale pour la Recherche (ANR) under grants ANR 09BLAN0283, ANR 11-JSV5-0002, ANR-14-CE09-0006, and ANR-12-BSV5001401, and by the Fondation pour la Recherche Médicale (FRM) under grant DEQ20120323737. F.R. acknowledges support from the EMBO (ALTF 577-2010). M.L. acknowledges support from the University of Chicago FACCTS program, Marie Curie Integration Grant PCIG12-GA-2012-334053, and “Investissements d’Avenir” LabEx PALM (ANR-10-LABX-0039-PALM).

REFERENCES

- Ridley, A. J., M. A. Schwartz, ..., A. R. Horwitz. 2003. Cell migration: integrating signals from front to back. *Science*. 302:1704–1709.
- Hotulainen, P., and P. Lappalainen. 2006. Stress fibers are generated by two distinct actin assembly mechanisms in motile cells. *J. Cell Biol.* 173:383–394.
- Pollard, T., and W. Earnshaw. 2008. *Cell Biology*. Saunders/Elsevier, Philadelphia, PA.
- Blanchoin, L., R. Boujemaa-Paterski, ..., J. Plastino. 2014. Actin dynamics, architecture, and mechanics in cell motility. *Physiol. Rev.* 94:235–263.

- Bornschlöggl, T., S. Romero, ..., P. Bassereau. 2013. Filopodial retraction force is generated by cortical actin dynamics and controlled by reversible tethering at the tip. *Proc. Natl. Acad. Sci. USA*. 110:18928–18933.
- Aratyn, Y. S., T. E. Schaus, ..., G. G. Borisy. 2007. Intrinsic dynamic behavior of fascin in filopodia. *Mol. Biol. Cell*. 18:3928–3940.
- Heintzelman, M. B., and M. S. Mooseker. 1992. Assembly of the intestinal brush border cytoskeleton. *Curr. Top. Dev. Biol.* 26:93–122.
- Roberts, W. M., J. Howard, and A. J. Hudspeth. 1988. Hair cells: transduction, tuning, and transmission in the inner ear. *Annu. Rev. Cell Biol.* 4:63–92.
- Janmey, P. A., S. Hvidt, ..., T. P. Stossel. 1994. The mechanical properties of actin gels. Elastic modulus and filament motions. *J. Biol. Chem.* 269:32503–32513.
- Heussinger, C., B. Schaefer, and E. Frey. 2007. Nonaffine rubber elasticity for stiff polymer networks. *Phys. Rev. E Stat. Nonlin. Soft Matter Phys.* 76:031906.
- Koenderink, G. H., Z. Dogic, ..., D. A. Weitz. 2009. An active biopolymer network controlled by molecular motors. *Proc. Natl. Acad. Sci. USA*. 106:15192–15197.
- Galkin, V. E., A. Orlova, ..., E. H. Egelman. 2010. Structural polymorphism in F-actin. *Nat. Struct. Mol. Biol.* 17:1318–1323.
- Galkin, V. E., A. Orlova, and E. H. Egelman. 2012. Actin filaments as tension sensors. *Curr. Biol.* 22:R96–R101.
- Bartles, J. R. 2000. Parallel actin bundles and their multiple actin-binding proteins. *Curr. Opin. Cell Biol.* 12:72–78.
- Tolomeo, J. A., and M. C. Holley. 1997. Mechanics of microtubule bundles in pillar cells from the inner ear. *Biophys. J.* 73:2241–2247.
- Trepac, X., G. Lenormand, and J. J. Fredberg. 2008. Universality in cell mechanics. *Soft Matter*. 4:1750–1759.
- Shin, J. H., L. Mahadevan, ..., P. Matsudaira. 2004. Bending stiffness of a crystalline actin bundle. *J. Mol. Biol.* 337:255–261.
- Ferrer, J. M., H. Lee, ..., M. J. Lang. 2008. Measuring molecular rupture forces between single actin filaments and actin-binding proteins. *Proc. Natl. Acad. Sci. USA*. 105:9221–9226.
- Schmoller, K. M., P. Fernández, ..., A. R. Bausch. 2010. Cyclic hardening in bundled actin networks. *Nat. Commun.* 1:134.
- Claessens, M. M., M. Bathe, ..., A. R. Bausch. 2006. Actin-binding proteins sensitively mediate F-actin bundle stiffness. *Nat. Mater.* 5:748–753.
- Bathe, M., C. Heussinger, ..., E. Frey. 2008. Cytoskeletal bundle mechanics. *Biophys. J.* 94:2955–2964.
- Strehle, D., J. Schnauss, ..., B. Gentry. 2011. Transiently crosslinked F-actin bundles. *Eur. Biophys. J.* 40:93–101.
- Faix, J., and K. Rottner. 2006. The making of filopodia. *Curr. Opin. Cell Biol.* 18:18–25.
- Schnauß, J., T. Golde, ..., J. A. Käs. 2016. Transition from a linear to a harmonic potential in collective dynamics of a multifilament actin bundle. *Phys. Rev. Lett.* 116:108102.
- Streichfuss, M., F. Erbs, ..., J. P. Spatz. 2011. Measuring forces between two single actin filaments during bundle formation. *Nano Lett.* 11:3676–3680.
- Lemièrre, J., K. Guevorkian, ..., T. Betz. 2013. α -Hemolysin membrane pore density measured on liposomes. *Soft Matter*. 9:3181–3187.
- Berg-Sørensen, K., and H. Flyvbjerg. 2004. Power spectrum analysis for optical tweezers. *Rev. Sci. Instrum.* 75:594–612.
- Romero, S., C. Le Clainche, ..., M. F. Carlier. 2004. Formin is a processive motor that requires profilin to accelerate actin assembly and associated ATP hydrolysis. *Cell*. 119:419–429.
- Michelot, A., E. Derivery, ..., L. Blanchoin. 2006. A novel mechanism for the formation of actin-filament bundles by a nonprocessive formin. *Curr. Biol.* 16:1924–1930.

30. Soeno, Y., H. Abe, ..., T. Obinata. 1998. Generation of functional β -actinin (CapZ) in an *E. coli* expression system. *J. Muscle Res. Cell Motil.* 19:639–646.
31. Lu, J., and T. D. Pollard. 2001. Profilin binding to poly-L-proline and actin monomers along with ability to catalyze actin nucleotide exchange is required for viability of fission yeast. *Mol. Biol. Cell.* 12:1161–1175.
32. Miyazaki, M., M. Chiba, ..., S. Ishiwata. 2015. Cell-sized spherical confinement induces the spontaneous formation of contractile actomyosin rings in vitro. *Nat. Cell Biol.* 17:480–489.
33. Köhler, S., O. Lieleg, and A. R. Bausch. 2008. Rheological characterization of the bundling transition in F-actin solutions induced by methylcellulose. *PLoS One.* 3:e2736.
34. Isambert, H., P. Venier, ..., M.-F. Carlier. 1995. Flexibility of actin filaments derived from thermal fluctuations. Effect of bound nucleotide, phalloidin, and muscle regulatory proteins. *J. Biol. Chem.* 270:11437–11444.
35. Broedersz, C. P., and F. C. MacKintosh. 2014. Modeling semiflexible polymer networks. *Rev. Mod. Phys.* 86:995–1036.
36. Ward, A., F. Hilitski, ..., Z. Dogic. 2015. Solid friction between soft filaments. *Nat. Mater.* 14:583–588.

Biophysical Journal, Volume 113

Supplemental Information

Adaptive Response of Actin Bundles under Mechanical Stress

Florian Ruckerl, Martin Lenz, Timo Betz, John Manzi, Jean-Louis Martiel, Mahassine Safouane, Rajaa Paterski-Boujemaa, Laurent Blanchoin, and Cécile Sykes

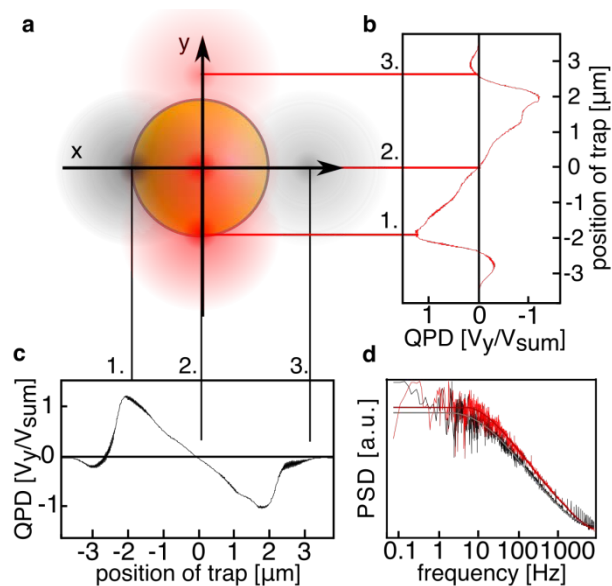


Figure S1: Schematic of trap calibration using time-shared multiple optical traps. (a) Illustration of the scanning motion of the traps. The intensity of the laser traps is collected by a four quadrant diode (QPD), allowing to determine the displacement of the bead in the trap. (b) and (c) Normalized voltage signal on the QPD in x- and y-direction (red and black curve, respectively). The linear region around the center is used to convert the recorded signal into the displacement of the bead in trap. The numbers 1-3 indicate the different positions of the trap with respect to the bead, and the corresponding signal on the QPD. (d) Power spectral density (PSD) calculated from the thermal motion of the bead in the trap. From these curves the trap stiffness is obtained in x- and y-direction following the procedure described by Berg-Sørensen and Flyvbjerg (1).

Figure S2: Time traces of several compression-expansion experiments at different speeds. (a)-(f) corresponds to trap velocities of 0.5, 1, 2, 5, 10, and 20 $\mu\text{m/s}$, respectively. All curves show similar features, namely a distinct buckling event in the first compression phase and a high degree of uniformity in the following cycles, indicating that the bundle reaches a steady state. Note that the model does not reproduce the initial sharp peak in the force curve in the three fastest compression experiments, suggesting that they may involve additional irreversible mechanisms, e.g., filament breaking. Red curves correspond to the fit described in the main text of the paper. Each curve corresponds to a different bundle, and one set of parameters τ , k_s and κ is used to fit each curve (see Table S1).

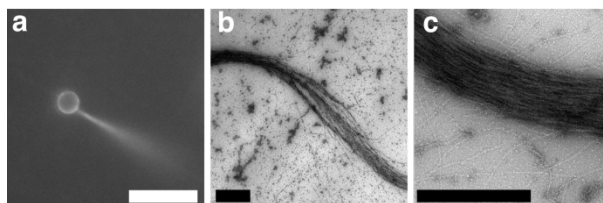


Figure S3: Fluorescent and electron microscopy images of actin bundles. (a) A typical image of a single bundle protruding from a mDia1 coated latex bead ($d=2\mu\text{m}$), the scale bar is $10\mu\text{m}$. (b-c) EM micrographs of an actin bundle. The average thickness of the bundle grown in solution (for details on the buffer see Materials and Methods) is estimated to be between 200 and 700nm. The scale bar is $1\mu\text{m}$ in both (b) and (c).

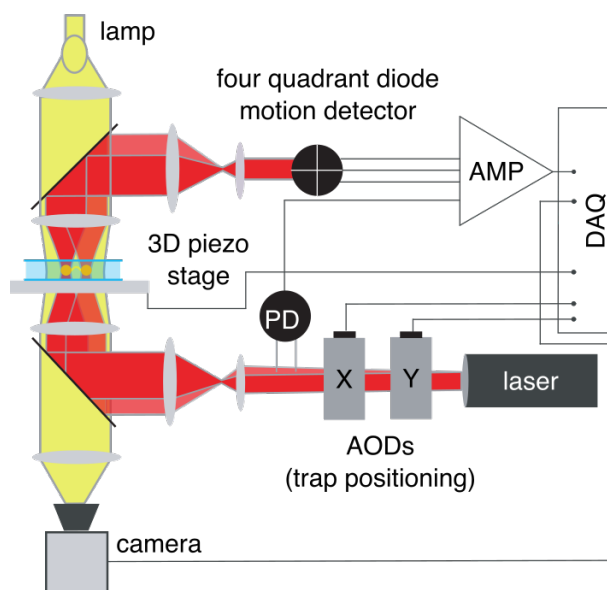


Figure S4: Schematic of the multiple optical tweezer setup. The position of the traps in the object plane is controlled by passing the IR through two computer controlled and perpendicularly oriented acousto-optical deflectors (AODs). Then the beam is widened to slightly overfill the back aperture of the focusing objective and the light is collected by a long distance objective. Positioning of the sample is achieved by a 3D piezo stage. The position of trapped beads is detected using a four-quadrant photo diode (QPD), connected to an amplifier. Two controller cards from National Instruments are used for data acquisition and setup control, allowing a sampling rate of 500kHz per channel of the QPD.

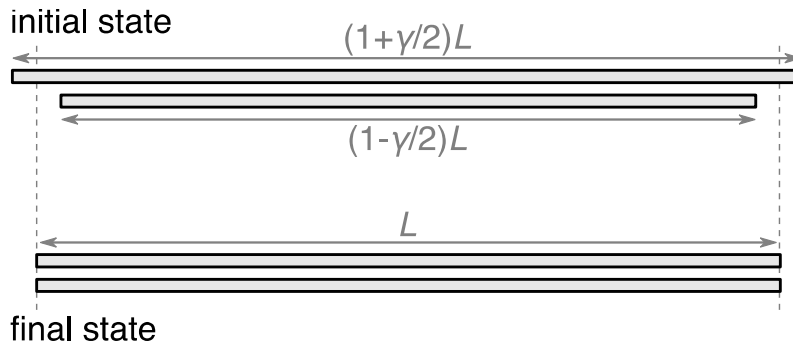


Figure S5: Minimal geometry for the relaxation of an inter-bundle strain. In the initial state, the top filament is stretched with a strain $\gamma/2$, while the bottom filament is compressed with a strain $-\gamma/2$. As discussed in the Supplemental text, the viscoelastic time τ is the characteristic time associated to the relaxation of the small relative strain γ .

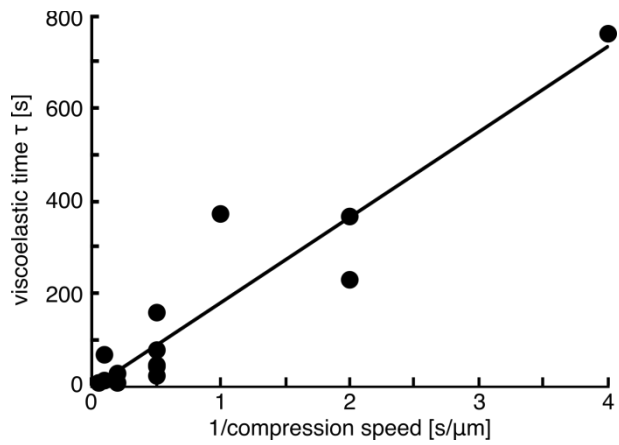


Figure S6: Dependency of the characteristic viscous time on compression speed, taken from the values of Table 1. Note that the viscoelastic time is obtained by fitting the experimental data with the model described in the main text. Pointing at further underlying complexity of the system. The line is a guide for the eye, illustrating the apparent proportionality between the viscoelastic time τ and the inverse compression speed.

Table S1 Parameters from the fits of data without waiting times, using the model described in the main text of the article. T is the driving period, L_0 the initial length of the bundle, κ the bending modulus, k_s the stretching modulus, and τ the viscoelastic time. The line with the asterisk indicates the data shown in Fig. 2. Note that each data set corresponds to a different bundle.

Trap speed [$\mu\text{m/s}$]	T [s]	L_0 [μm]	κ [$\text{pN } \mu\text{m}^2$]	k_s [pN]	τ [s]	Max. Strain
0.25	40.0	36.93	1179.4	64.4	765.6	0.117
0.5	80.0	30.29	344.2	19.0	231.4	0.613
0.5	80.0	34.91	299.8	51.8	370.4	0.548
*1.0	40.0	34.92	687.9	54.3	375.5	0.527
2.0	20.0	34.93	302.1	85.3	42.8	0.548
2.0	20.0	34.91	426.9	114.6	77.5	0.544
2.0	20.0	34.96	689.3	72.2	161.8	0.528
2.0	8.0	36.93	747.4	168.7	46.0	0.187
2.0	5.0	36.92	871.7	254.8	24.5	0.106
5.0	8.0	33.03	637.4	174.9	22.7	0.542
5.0	8.0	34.93	461.6	141.7	30.0	0.540
5.0	2.0	36.94	1785.3	174.9	9.5	0.101
10.0	4.0	34.96	574.4	202.5	13.1	0.530
10.0	4.0	34.95	2175.1	31.9	68.7	0.469
20.0	2.0	34.97	695.8	233.8	6.7	0.509

Supplemental Information

Fitting of the viscoelastic model to experimental data

To determine the bundle's viscoelastic parameters, we fit the model described in equations [1-3] (see main text) to the experimentally obtained force curves [*e.g.*, that of Fig. 2a]. We substitute the expressions of σ_L , σ_θ and f from equations [2] and [3] into equation [1] to obtain a system of two nonlinear differential equations for two unknown functions $L(t)$ and $\theta(t)$. We solve this system numerically using Mathematica's numerical differential equation solver while driving the model with a function $X(t)$ (representing the distance between the centers of the two optical traps) identical to that used in the experiment. We then use equation [3] to compute the function $f(t)$ from the solutions $L(t)$ and $\theta(t)$, and compute the mean square distance between $f(t)$ and the measured experimental force curve. We repeat the operation to minimize this mean square distance over experimental parameters k_s , κ and τ according to Mathematica's derivative-free principal axis method (2).

Estimate of the number of filaments in the bundle and if they are weakly or strongly coupled

The buckling force F_B of a bundle made out of N filaments of initial length L_0 is given by (3):

$$F_B = \frac{\pi^2 k_B T L_p}{L_0^2} = \frac{\pi^2 k_B T N^c l_p}{L_0^2}, \quad [4]$$

where $L_p = \kappa/k_B T$ is the persistence length of the bundle, l_p the persistence length of a single actin filament. The exponent c varies between 1 and 2 depending on whether the filaments are weakly ($c = 1$), or strongly ($c = 2$) coupled (4). In the strongly-coupled limit, the filaments are held in register with respect to each other, similar to rows of atoms in a single metallic beam. Conversely, in a weakly

coupled bundle, filaments may come out of register, and the bending rigidity of the beam is the sum of those of the filaments, with no dramatic contribution from the couplings. Previous reports show that c approaches 2 for bundles stabilized by depletion agents (4).

To assess whether the internal bundle mechanics probed here is more consistent with weak or strong interactions, we use equation [4] to infer the typical number of filaments in our bundle from our measurement of its bending modulus as $N = (\kappa/k_B T l_p)^{1/c}$. Using our measured average $\kappa \simeq 770 \text{ pN} \cdot \mu\text{m}^2$ and the value $l_p \simeq 10 \mu\text{m}$, we consider the two extreme cases of strong interactions ($c = 2$), and weak interactions ($c = 1$), yielding $N_{c=2} \simeq 140$, and $N_{c=1} \simeq 19,000$, respectively. These widely different estimates, are consistent with widely different bundle radii: the strong binding hypothesis should yield a relatively thin bundle with radius $r_{\text{bundle}} \simeq r_{\text{F-actin}} \sqrt{N_{c=2}} \simeq 35 \text{ nm}$, where we used $r_{\text{F-actin}} \simeq 3 \text{ nm}$ for the radius of a single actin filament. On the other hand, the weak binding hypothesis implies a much thicker bundle radius $r_{\text{bundle}} \simeq r_{\text{F-actin}} \sqrt{N_{c=1}} \simeq 420 \text{ nm}$.

These values correspond to a bundle thickness of $r_{\text{bundle}} \simeq r_{\text{F-actin}} \sqrt{N_{c=2}} = 35 \pm 4 \text{ nm}$ and $r_{\text{bundle}} \simeq r_{\text{F-actin}} \sqrt{N_{c=1}} = 416 \pm 94 \text{ nm}$, respectively, in agreement with the above estimates from the model.

We discriminate between these two hypotheses through direct inspection of the bundles in electron microscopy, which reveal a bundle diameter $r_{\text{bundle}} \simeq 200 - 700 \text{ nm}$ (see supplemental Fig. S3). We conclude that filaments within the bundle are weakly coupled.

Inter-filament friction coefficient estimate

To compare the magnitude of the friction in our experiments and in Ref. (5), we compute and orders of magnitude for the friction coefficients associated with each study. We first consider two filaments that

translate relative to each other with a uniform velocity v , and define the friction coefficient ζ between two filaments through

$$f = -\zeta L v, \quad [5]$$

where L is the length of the overlap between the two filaments, and f is the friction force between them. The viscoelastic relaxation time τ introduced in the main text is the typical time required to relax a differential stretching between the two filaments in the presence of such a friction, as illustrated in Fig. S5. In the configuration considered, the elastic energy associated to either one of the filaments reads

$$E = \frac{k_s}{2} \left(\frac{\gamma}{2}\right)^2, \quad [6]$$

while the power dissipated at the interface between the two filaments is the work performed by the friction force f , namely

$$P = \int_{-L/2}^{L/2} \zeta v(s)^2 ds, \quad [7]$$

where $v(s)$ denotes the (non-uniform) relative velocity between the two filaments at the curvilinear coordinate s . As the present calculation only intends to provide an order-of-magnitude estimate of the bundle viscoelastic time, in the following we use the simplifying assumption that filaments deform affinely, implying $v(s) = s \frac{d\gamma}{dt}$ to first order in γ .

Let us now consider a full close-packed bundle, where each filament has six neighbors with mismatched lengths. In such a situation, there are three times as many filament-filament interfaces as there are filaments. Balancing the power dissipated through friction with the change in elastic energy of the bundle, we thus obtain

$$\frac{dE}{dt} = -3P. \quad [8]$$

Inserting the expressions of E and P into this equation, we find that the strain γ evolves according to:

$$\frac{d\gamma}{dt} = -\frac{8k_s}{\zeta L^2} \gamma, \quad [9]$$

implying an exponential relaxation with viscoelastic time

$$\tau = \frac{\zeta L^2}{8k_s}. \quad [10]$$

Using the average values measured in our study, namely $k_s = 120$ pN, $\tau = 150$ s and $L = 35$ μm , we invert this relation to compute an inter-filament friction coefficient $\zeta \simeq 117$ $\text{N} \cdot \text{s} \cdot \text{m}^{-2}$. By comparison, Ref. (5) reports typical friction forces of the order of $f = 5$ pN for filaments overlapping over a length $L = 2$ μm and sliding at speeds $v = 100$ $\text{nm} \cdot \text{s}^{-1}$, yielding a friction coefficient of the order of $\zeta \simeq 25$ $\text{N} \cdot \text{s} \cdot \text{m}^{-2}$. Despite the substantial differences in geometry and confinement of the filaments, it thus appears that the frictional forces encountered in our study are of the same order of magnitude as those previously reported in Ref. (5).

Variability of the characteristic viscoelastic time τ

While the short-time, elastic properties of the bundle are well-explained by combining the known elastic characteristics of individual filaments with a weak-binding hypothesis, their viscoelastic behavior proves to be more complex. In classical Maxwell models the viscoelastic time of the material is a material property independent on the frequency at which it is driven. In contrast, we show in Fig. S5 that in our bundles, the parameter τ appears to decrease with increasing driving frequency, *i.e.*, a higher compression speed. Assuming that the critical strain required for buckling is similar in all experiments presented in Fig. S2, the time to reach it (the visco-elastic time) is inversely proportional to the bundle compression velocity.

Bibliography:

1. Berg-Sørensen, K., and H. Flyvbjerg. 2004. Power spectrum analysis for optical tweezers. *Review of Scientific Instruments* 75:594-612.
2. Brent, R. P. 1973. Algorithms for minimization without derivatives. Prentice Hall (reprinted by Dover, 2002 and 2013).
3. Landau, L. D., L. P. Pitaevskii, A. M. Kosevich, and E. M. Lifshitz. 2012. Theory of Elasticity. In 123Library. Butterworth-Heinemann.
4. Claessens, M. M., M. Bathe, E. Frey, and A. R. Bausch. 2006. Actin-binding proteins sensitively mediate F-actin bundle stiffness. *Nat Mater* 5:748-753.
5. Ward, A., F. Hilitski, W. Schwenger, D. Welch, A. W. Lau, V. Vitelli, L. Mahadevan, and Z. Dogic. 2015. Solid friction between soft filaments. *Nat Mater* 14:583-588.